Solution Structure of the SH3 Domain from Bruton's Tyrosine Kinase[†,‡]

Henrik Hansson,[§] Pekka T. Mattsson,[||,⊥,▽] Peter Allard,[§] Pekka Haapaniemi,[||,⊥] Mauno Vihinen,[#] C. I. Edvard Smith,[⊥,▽] and Torleif Härd*[,§]

Center for Structural Biochemistry, Department of Biochemistry and Biotechnology, Royal Institute of Technology, Novum, S-141 57 Huddinge, Department of Biochemistry and Food Chemistry, University of Turku, Vatselankatu 2, Arcanum, FIN-20014 Turku, Finland, Center for BioTechnology, Department of Biosciences at Novum, Karolinska Institute, S-141 57 Huddinge, Sweden, Department of Immunology, Microbiology Pathology and Infectious Deseases (IMPI), Karolinska Institute, Huddinge University Hospital, S-141 86 Huddinge, Sweden, and Department of Biosciences, Division of Biochemistry, University of Helsinki, P.O. Box 56, FIN-00014 Helsinki, Finland

Received September 29, 1997

ABSTRACT: X-linked agammaglobulinemia (XLA) is a heritable immunodeficiency caused by mutations in the gene coding for Bruton's tyrosine kinase (Btk). Btk belongs to the Tec family of tyrosine kinases. Each member of the family contains five regions and mutations causing XLA have been isolated in all five regions. We have determined the solution structure of the Src homology 3 (SH3) domain of Btk using two- and three-dimensional nuclear magnetic resonance (NMR) spectroscopy on natural abundance and ^{15}N-labeled protein material. The structure determination is complemented by investigation of backbone dynamics based on ^{15}N NMR relaxation. The Btk SH3 forms a well-defined structure and shows the typical SH3 topology of two short antiparallel β-sheets packed almost perpendicular to each other in a sandwich-like fold. The N- and C-termini are more flexible as are peptide fragments in the RT and n-Src loops. The studied Btk SH3 fragment adopts two slowly interconverting conformations with a relative concentration ratio of 7:1. The overall fold of the minor form is similar to that of the major form, as judged on the basis of observed NOE connectivities and small chemical shift differences. A tryptophan (W251) ring flip is the favored mechanism for interconversion, although other possibilities cannot be excluded. The side chain of Y223, which becomes autophosphorylated upon activation of Btk, is exposed within the potential SH3 ligand binding site. Finally, we compare the present Btk SH3 structure with other SH3 structures.

The immunodeficiency X-linked agammaglobulinemia (XLA) is caused by a lymphocyte differentiation block resulting in no or very low concentrations of B cells and plasma cells (*1*). The defective gene codes for Bruton's tyrosine kinase, Btk, a cytoplasmic tyrosine kinase and a member of the Tec family of nonreceptor tyrosine kinases (*2*, *3*). It appears to play an important role in the regulation of B cell proliferation and differentiation. Btk is expressed in most hematopoietic cells, but is selectively downregulated in plasma cells and T-lymphocytes (*4*−*6*). The domain organization of Btk and of other Tec family tyrosine kinases resembles that of the Src family tyrosine kinases in that they all have a Src homology 3 (SH3) domain, an SH2 domain and a C-terminal catalytic (kinase) domain. Tec family kinases lack the consensus N-terminal myristoylation site of Src family kinases but have an N-terminal pleckstrin homology (PH) domain (*7*) that might play a role in membrane translocation of the kinase (*8*). The PH domain is followed by a Tec homology (TH) domain/region (*6*, *9*). XLA-causing mutations have been found in exons encoding all five subdomains (*10*). Among these is a point mutation in a 5′ splice site, resulting in a deletion of 21 C-terminal residues in the SH3 domain, including parts of the potential ligand-binding site (*11*). Circular dichroism studies on a peptide corresponding to the SH3 domain part of this deletion mutant suggest that it does not alone form a folded structure (*12*).

SH3 domains are known to interact with proline rich motifs with the consensus sequence PXXP (*13*, *14*). All known SH3-ligands contain at least one PXXP motif. The TH domain of Btk contains two such regions, which interact with the SH3 domains of Lyn, Fyn, and Hck (*15*) whereas the related Tec family kinases Bmx, Itk, and Tec contain one such sequence (*9*, *16*). It has been shown that the corresponding sequence in Itk can form an intramolecular complex with the SH3 domain and that this complex inhibits binding of the SH3 domain and the proline-rich motif to their ligands (*17*).

[†] This work was supported by the Swedish Structural Biology Network (SBNet), the Swedish Natural Sciences Research Council, the Swedish Cancer Society, the Swedish Medical Research Council, the Biocentrum Helsinki, and the Academy of Finland.

[‡] The atomic coordinates for the structures described in this paper have been submitted to the Brookhaven Protein Data Bank (accession codes are 1aww and 1awx).

* To whom correspondence should be addressed.
[§] CSB Novum.
[||] University of Turku.
[⊥] CBT Novum.
[▽] IMPI.
[#] University of Helsinki.

[1] Abbreviations: XLA, X-linked agammaglobulinemia; Btk, Bruton's tyrosine kinase; SH3, Src homology 3; PH, Pleckstrin homology; TH, Tec homology; IPTG, isopropyl D-thiogalactopyranoside; GF-HPLC, gel filtration high-performance liquid chromatography; SA, simulated annealing; rmsd, root-mean-square deviation.

S0006-2960(97)02409-4 CCC: $15.00
Published on Web 02/10/1998

Recently the crystal structures of inactivated forms of c-Src and Hck tyrosine kinases were solved (*18*, *19*). These structures reveal intramolecular interactions between the catalytic domain and both the SH2 and the SH3 domains. The linker region between the SH2 domain and the catalytic domain forms a left-handed PPII helix, which acts as a ligand for the SH3 domain. Activation of Src family kinases involves a displacement of the SH3 domain (*20*).

A regulatory C-terminal tyrosine of Src family kinases is not present in Btk or Tec family kinases. Thus, the regulation of Btk must be partially different from that of the Src family kinases. Btk is activated by a phosphorylation of a conserved tyrosine (Y551) within the catalytic domain (*21*). The activated Btk, which is predominantly membrane associated, is then autophosphorylated at Y223 within the SH3 domain (*22*).

Our objective is to characterize the structure and function of Btk at a molecular level to understand the mechanism of regulation and how a defective enzyme can result in XLA. As a part of these studies we have determined the solution structure of the human Btk SH3 domain using nuclear magnetic resonance (NMR) methods. The backbone conformation of Btk SH3 is compared to that of other SH3 domains, and the position of Y223 in the structure is discussed in relation to its role in Btk function.

MATERIALS AND METHODS

Cloning and Purification of Btk SH3. The DNA fragment encoding residues 212−275 of human Btk was amplified by PCR, and the fragment was cloned into the pGEX-4T-3 vector (Pharmacia, Sweden) for expression in *Escherichia coli*. The construct was transformed in the XL1-Blue strain of *E. coli* (*23*), and Btk SH3 was expressed by fermenting the cells in 2×TY medium containing 2% glucose as a catabolic repressor at 37 °C until the absorbance at 600 nm reached 1.8−2.0. The protein expression was induced by addition of isopropyl D-thiogalactopyranoside (IPTG) to a final concentration of 0.1 mM. After 3−4 h of induction the cells were harvested and lysed by sonication at 4 °C in a PBS buffer containing 1% Triton X-100, 0.1 mM aprotinin, 1 mM leupeptin, 1 mM EDTA, and 0.2 mg/mL lysozyme. The lysate was cleared by centrifugation at 18000*g* for 40 min. The GST-fusion product was bound to glutathione-Sepharose, and digested with thrombin (50 units; Sigma Chemical Co.), and Btk SH3 was eluted with PBS buffer. The digested and eluted Btk SH3 contained three extra residues in the N-terminal, denoted G1, S2, and M3. The purification was continued using Q-Sepharose FF (Pharmacia, Sweden) equilibrated with phosphate buffer (20 mM sodium phosphate and 50 mM NaCl at pH 6.5). The protein was then eluted with a linear 0.05−0.5 M salt gradient. Fractions containing Btk SH3 were pooled and concentrated for gel filtration on a Superdex 75 column (Pharmacia, Sweden) equilibrated with phosphate buffer. The gel-filtrated Btk SH3 was finally concentrated to 5 mg/mL, sodium azide was added to a final concentration of 0.02%, and the protein solution was stored at 4 °C. The ^{15}N-labeled protein was expressed in M9 minimal medium with $^{15}NH_4Cl$ (0.5 g/L; Isotec Inc., OH) and ISOGRO ^{15}N Powder-Growth Medium (1 g/L; Isotec Inc., OH) and purified as the unlabeled protein, but with an extra gel filtration.

Analytical Methods. The Btk SH3 domain was identified using matrix-assisted laser desorption mass spectroscopy and N-terminal sequencing. The purity of the protein was analyzed by gel filtration high-performance liquid chromatography (GF−HPLC) using a Tosohaas TSK-GEL G3000 SWXL column (7.8 × 300 mm) equilibrated with phosphate buffer. The protein concentration was measured using the Bradford method (*24*) with bovine gammaglobulins (Sigma Chemical Co., St. Louis, MO) as standard.

NMR Sample Preparation. The samples containing Btk SH3 were further concentrated using Amicon Ultrafiltration cells with Amicon Diaflo membranes (YM3) and Amicon Centricon 3 concentrators. Three samples were used for NMR resonance assignments and structure determination: ^{15}N-labeled protein in H_2O/D_2O (9:1), unlabeled protein in H_2O/D_2O (9:1) and unlabeled protein in 100% D_2O. All NMR samples were prepared in 20 mM phosphate buffer, 100 mM NaCl, and 0.1 mM EDTA at pH 6.5. Final protein concentrations were approximately 2 and 8−10 mM for ^{15}N-labeled and unlabeled samples, respectively. The purity of NMR samples was checked with SDS−PAGE.

NMR Spectroscopy. NMR was measured using a Varian Unity 500 NMR spectrometer (at a magnetic field of 11.7 T) equipped with three rf channels, pulsed field gradients, and a 5 mm triple-resonance (^{1}H/^{15}N/^{13}C) probe. Proton and ^{15}N chemical shifts at 30 °C were referenced to H_2O at 4.74 ppm and to external [^{15}N]benzamide at 105.4 ppm (*25*), respectively.

Two-dimensional homonuclear experiments, DQF-COSY (*26*), NOESY (*27*), and clean-TOCSY (28), were recorded at 30 °C with the H_2O/D_2O (9:1) and 100% D_2O samples and at 40°C with the H_2O/D_2O (9:1) sample. The data sets contained 512 t_1 increments and 32 transients/increment for the NOESY and DQF−COSY experiments, and 512 t_1 increments and 16 transients/increment for the TOCSY experiments, with 1024 acquired complex data points/transient in all experiments. The cross-relaxation mixing times used in various NOESY experiments ranged between 60 and 200 ms. In addition, NOESY spectra with 200, 500, and 750 ms mixing times were recorded at 50 °C on a protein sample in H_2O/D_2O. The isotropic mixing times used in the TOCSY experiments were 50 and 70 ms. Water suppression was achieved by presaturation during relaxation and cross-relaxation delays. In one 150 ms NOESY experiment, water suppression was achieved using the flip-back WATERGATE method according to Lippens et al. (*29*). The data were recorded in phase-sensitive mode with the hypercomplex States-TPPI method (*30*).

Two-dimensional and three-dimensional heteronuclear (^{1}H and ^{15}N) experiments, 2D HSQC (*31*, *32*), ^{15}N-edited TOCSY-HSQC, ^{15}N-edited NOESY-HSQC, and ^{15}N-edited HSQC-TOCSY-NOESY-HSQC (*32*) were recorded at 30 °C. The ^{1}H and ^{15}N transmitter frequencies were set to the resonance frequency of water and 119.6 ppm, respectively. Spectral widths were 5988 Hz in the *F*1 (^{1}H) dimension, 2000 Hz in the *F*2 (^{15}N) dimension (*F*1 for 2D HSQC), and 5999.7 Hz in the *F*3 (^{1}H) dimension (*F*2 for 2D HSQC). The 3D spectra were acquired with 128 t_1 increments, 32 t_2 increments, 8 transients/increment (4 in the 3D TOCSY−HSQC experiments) and 512 complex data points/transient (64 × 32 × 16 × 512 for HSQC-TOCSY-NOESY-HSQC) using sensitivity-enhanced detection (31). The cross-

relaxation mixing times for NOESY-HSQC were 75 and 150 ms, and the isotropic mixing times for TOCSY-HSQC were 27.2, 52.3, and 77.2 ms. The cross relaxation and isotropic mixing times in the HSQC-TOCSY-NOESY-HSQC were 150 and 28.7 ms, respectively.

Three-dimensional heteronuclear 3D HNHA with water flip-back (*33*) and 3D HNHB (*34*) with spin lock pulses and presaturation for suppression of the water signal were recorded at 30 °C. Transmitter frequencies, spectral widths, data set sizes, etc. were identical with those described above. Quadrature detection in indirectly detected dimensions was accomplished using the States-TPPI method.

Longitudinal and transverse relaxation rates (R_1 and R_2) of backbone ^{15}N nuclei and the $\{^1H\}^{15}N$ steady-state NOE were measured using HSQC-based pulse sequences that suppress cross-correlation between $^{15}N-^1H$ dipolar interactions and ^{15}N chemical shift anisotropy and which avoid unnecessary water saturation (Figure 10a−c in Farrow et al. (*35*)). The measurements were performed at 30 °C. The spectral widths were 8000 Hz in the ^{1}H dimension and 2000 Hz in the ^{15}N dimension. The ^{1}H and ^{15}N transmitter frequencies were set to 4.74 and 119.6 ppm, respectively. The spectra were acquired with 128 t_1 increments of 512 complex points using sensitivity-enhanced detection in the ^{15}N dimension. In the case of the R_1 and R_2 measurements, the pulse delay (between transients) was set to 1.6 s, 4 scans were added for each FID, and the data accumulation was preceded by 32 steady-state transients. The CPMG spin−echo delay in the transverse relaxation rate measurement was 450 ms. In the case of the steady-state NOE measurement the pulse delay was set to 5 s, with or without 3 s of ^{1}H saturation, with 8 scans added for each FID and 8 steady-state transients before the first t_1 increment. Delays used for the R_1 measurements were 11.0, 121.3, 231.5, 341.7, 452.0, 562.5, 672.5, and 1334 ms. The delays used for R_2 measurements were 33.2, 66.4, 99.6, 132.9, 166.1, 199.3, and 265.7 ms. The relaxation experiments were carried out with these relaxation delays in random order.

The NMR data, except for the NMR relaxation data (see below), were processed using Varian software (VNMR 4.3 and 5.2) running on SUN Sparc workstations. Processed 2D and 3D spectra normally contained 2048 × 2048 and 512 × 64 × 1024 real data points, respectively. Spectral analysis was performed with the interactive graphics computer program ANSIG v. 3.2 (*36*, *37*).

Evaluation of Relaxation Data. NMR spectra were processed and evaluated using Felix version 2.3 on a Silicon Graphics Indy workstation. The spectra were processed using cosine and cosine-squared window functions, and the baseline was corrected in the ^{1}H dimension. Felix macros and FORTRAN programs from the package ModelFree 3.1 (Drs. M. Akke and A. Palmer, III, Columbia University; *38*) were used for data extraction and evaluation. Resonance intensities were obtained as peak heights. Noise levels were obtained from repeated experiments, and random errors in measured relaxation rates were estimated using Monte Carlo simulations (*38*). The error in the steady-state NOE measurements was estimated by repeating the measurement once. The average steady-state NOE of the two measurements is presented.

The relaxation data were quantified using well-known relations between relaxation rates and spectral densities (*39*). The spectral density function derived by Lipari and Szabo (*40*, *41*) was applied to interpret experimental data in terms of physically meaningful parameters. First, the overall rotational correlation time was estimated to be $\tau_c = 5.5$ ns from the average R_1/R_2 ratio for the structured peptide fragments V219−L244 and W251−E271. This procedure to obtain τ_c is motivated because the R_1/R_2 ratio is sensitive to τ_c, but insensitive to the generalized order parameter, S^2, and internal correlation time, τ_e, if internal motions are restricted, i.e., when $S^2 > 0.7$. Residue-specific S^2 and τ_e values were then calculated from measured R_1 rates and $\{^1H\}^{15}N$ NOEs and the calculated τ_c by minimizing a sum-of-squares target function for each residue i: $\chi_i^2 = (R_{1,\mathrm{exp},i} - R_{1,\mathrm{calc},i})^2/\sigma_{R_1,i}^2 + (\mathrm{NOE}_{1,\mathrm{exp},i} - \mathrm{NOE}_{1,\mathrm{calc},i})^2/\sigma_{\mathrm{NOE},i}^2$ where indices "exp" and "calc" represent experimentally and back-calculated values, respectively, and σ is the experimental standard deviation. Errors in S^2 and τ_e were estimated in each case on the basis of Monte Carlo simulations in which normal distributions with $R_{1,\mathrm{exp}}$ and $\mathrm{NOE}_{1,\mathrm{exp}}$ as mean values and $\sigma_{R_1}^2$ and σ_{NOE}^2 as variances were assumed.

NOE Distance Restraints. Distance restraints were quantified from NOEs assigned in a 3D ^{15}N-edited NOESY-HSQC spectrum recorded with a 75 ms cross-relaxation mixing time and in 2D NOESY spectra with 60 ms mixing time. Most NOEs involving aromatic side chains were assigned in a 60 ms NOESY spectrum recorded in D_2O. Ambiguities in the NOE assignments could be resolved either in spectra obtained at 40 °C or by inspection of preliminary structures. The conversion of NOE cross-peak volumes into distances was based on calibration of observed NOEs typical for β-sheets against known distances within regular β-sheets (*42*). The NOE data were classified into three groups: strong, medium and weak, corresponding to distance limits of 1.8−2.8, 1.8−3.5, and 1.8−5.0 Å, respectively. NOE assignments and volume integrations were made within the ANSIG program (*36*, *37*). Pseudoatom and multiplicity corrections of NOEs involving methyls or equivalent groups, i.e., methylene or diastereotopic groups, were carried out according to Fletcher et al. (*43*).

Dihedral Angle Restraints and Stereospecific Assignments. Restraints for Φ dihedral angles were derived from $^3J_{\mathrm{HNH}^\alpha}$ coupling constants measured in the 3D HNHA spectrum (33); for $^3J_{\mathrm{HNH}^\alpha} > 8$ Hz, the Φ dihedral angle was restrained to $-120(\pm60)°$, and for $^3J_{\mathrm{HNH}^\alpha} > 9$ Hz the Φ dihedral angle was restrained to $-120(\pm40)°$ (*44*). No corrections for differential relaxation effects were made. Heteronuclear couplings, $^3J_{\mathrm{NH}^\beta}$, measured in 3D HNHB (*34*), and $^3J_{\alpha\beta}$, estimated from short mixing time ^{15}N-edited TOCSY spectra, in combination with observed short mixing time NOE intensities, were used to define χ^1 rotamers and assign β-methylene hydrogens stereospecifically (*45*).

Stereospecific assignments of the $C^\gamma H_3$ groups and identification of the χ^1 rotamer in a valine residue were made by analyzing the $^3J_{\mathrm{H}^\alpha\mathrm{H}^\beta}$ coupling constant in a DQF−COSY spectrum and the intensities of NOEs between H^γ and H^N protons in a 2D NOESY spectrum.

Structure Calculations. Structure calculations and analyses were carried out on a Digital DEC Alpha computer with parallel processors and Silicon Graphics Indy and Indigo workstations using X-PLOR 3.1 (*46*), InsightII v. 2.3.0 (Biosym Technologies, San Diego, CA), and Procheck-NMR (*47*). Structures were calculated and refined with X-PLOR

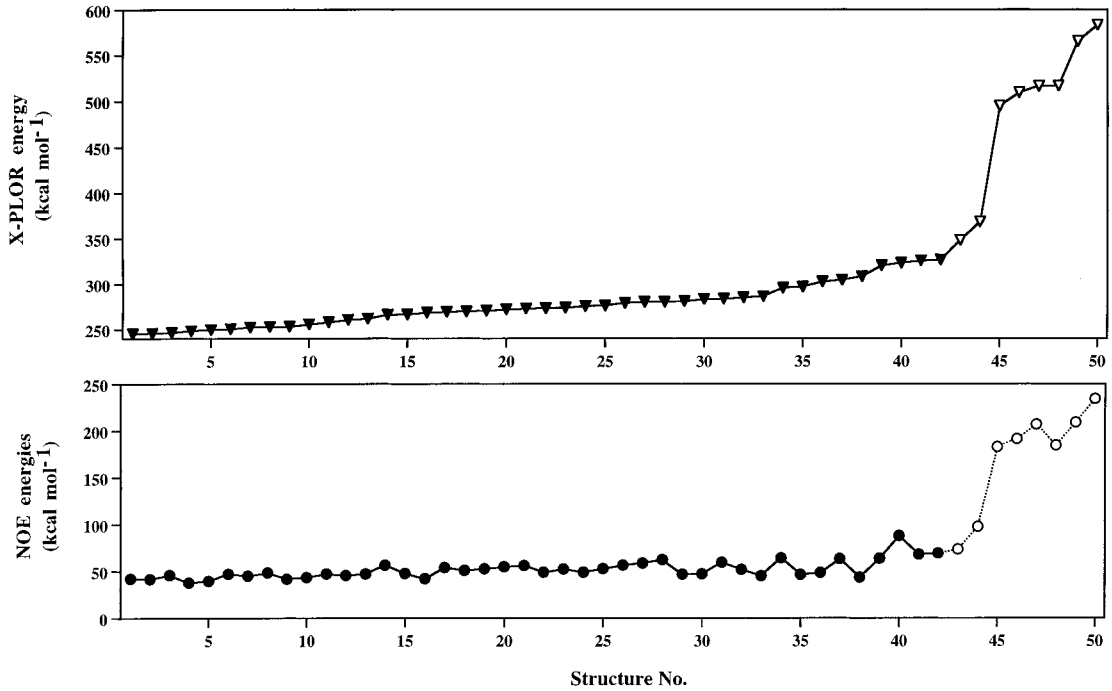

FIGURE 1: Energies of refined simulated annealing (SA) structures. (A) X-PLOR total energies for 50 SA structures arranged in order of increasing energy. The 42 selected structures, ⟨SA⟩, are represented with filled triangles. (B) NOE energy for the 50 structures arranged in the same order as in Figure 1A. ⟨SA⟩ ensemble structures are represented by filled circles.

using the *ab initio* simulated annealing (SA) protocol, "sa.inp", and SA refinement protocol, "refine.inp" (pages 311−314 and 316−319, respectively, in ref 46). Extended peptide conformations were used as starting structure for the *ab initio* SA.

All force constants, parametrization of potentials, molecular parameters, etc. were set to their default values, as in the original sa.inp and refine.inp protocols, throughout the calculations, with the exception of the van der Waals radii scale factor ("repel"), which was decreased to 0.8 (instead of to 0.75) during the final cooling stages in the refinement. A center averaging pseudoatom correction was used for all distance restraints. The temperature in sa.inp was initially set to 1500 K, and it was decreased in steps of 50 K (1.07 ps/step) during cooling to 100 K. The structures generated by the SA procedure were refined using SA refinement in two steps. In the first step the annealing temperature was set to 1000 K followed by cooling to 100 K in steps of 50 K (1.11 ps/step). In the second step, additional distance restraints from hydrogen bonds were added (see below) and the temperature of the system was raised to 400 K followed by cooling to 100 K (steps of 25 K, 1.67 ps/step). The SA refinement was followed by 2500 steps of Powell energy minimization.

From an ensemble of 50 calculated structures, 42 converged structures were selected on basis of the total energy (Figure 1A). This selected ensemble is denoted ⟨SA⟩. An average structure, SA_{ave}, was calculated by averaging superimposed coordinates. This average structure was energy minimized (and denoted $SA_{ave-min}$) using the same procedure and potentials as in the last energy minimization of the ensemble structures. The structures in ⟨SA⟩ were analyzed with respect to precision of atomic positions and dihedral angles, restraint violations, deviations from idealized bond geometries, and nonbonded interaction potentials and was further characterized with respect to backbone conformation and hydrogen bonds. The ensemble structures were searched for intramolecular backbone hydrogen bonds using the following two criteria: a distance between the donor hydrogen and the acceptor oxygen of less than 2.5 Å and a donor nitrogen−hydrogen−acceptor oxygen bond angle larger than 90°. Hydrogen bonds that fulfilled these criteria in a majority of the ensemble structures were then included as distance restraints in the final refinement step. Two distance restraints were added for each hydrogen bond: one for the distance between the donor hydrogen and acceptor oxygen (1.8−2.4 Å) and one for the distance between donor nitrogen and acceptor oxygen (2.6−3.2 Å). The hydrogen bonds used in the final refinement are reported in Table 1 together with a few additional hydrogen bonds that could be resolved in the final ensemble.

Table 1: Observed Backbone Hydrogen Bonds

donor residue (amide proton)	acceptor residue (oxygen)	no. of structures in which the hydrogen bond is observed
219 Val	241 Tyr	42
221 Ala	239 Asp	42
223 Leu	268 Tyr	42
235 Leu[a]	225 Tyr[a]	42
235 Leu[a]	233 Leu[a]	29
238Gly[a]	221 Ala[a]	34
241 Tyr	219 Val	42
242 Phe	255 Arg	42
252 Trp	264 Ile	42
255 Arg	242 Phe	42
256 Asp	260 Gln	42
262 Gly	254 Ala	42
266 Ser	250 Pro	42
268 Tyr[a]	265 Pro[a]	22
269 Val[a]	265 Pro[a]	26
270 Thr	220 Val	42

[a] These hydrogen bonds were not used as distance restraints but were clearly resolved after the last refinement.

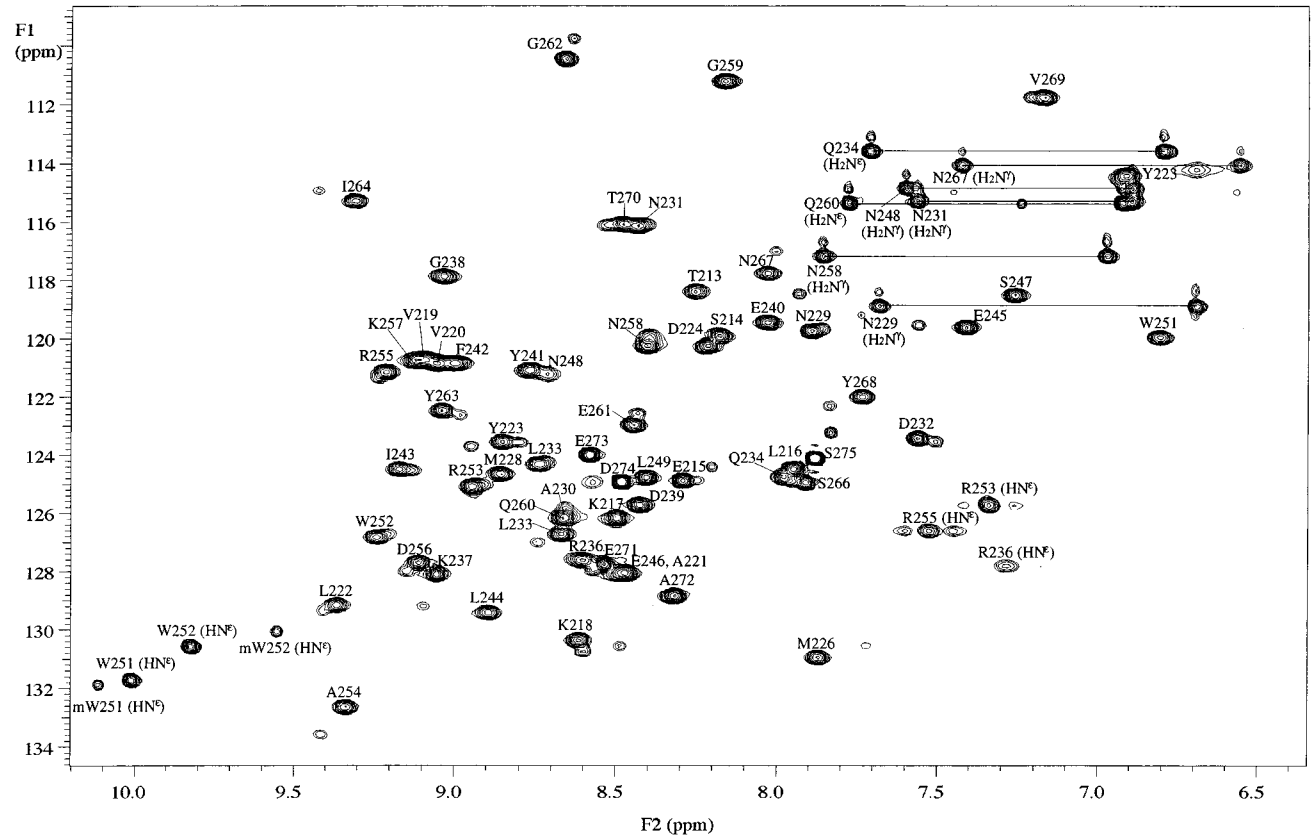

FIGURE 2: Assigned $^1H-^{15}N$ HSQC spectrum of ^{15}N-labeled Btk SH3. Minor form assignments (m) have been indicated only for tryptophan side-chain resonances. Amino group resonances of Asn and Gln side chains are connected by horizontal lines.

Dihedral angle order parameters, S^{angle}, were calculated according to Hyberts et al. (*48*). A value of S^{angle} approaching unity indicates a very well-defined dihedral angle whereas $S^{angle} = 42^{-1/2} = 0.154$ (for 42 structures) corresponds to an isotropic distribution.

Sequence Alignments and Structural Comparisons. The sequence of Btk SH3 was aligned with sequences of SH3 domains from Itk, c-Src, Fyn, Grb2, Lck, and Abl. Atomic coordinates for c-Src, Fyn, and Grb2 were obtained from the Brookhaven Protein Data Bank except for the Itk SH3 coordinates, which were kindly provided by Amy Andreotti at Howard Hughes Medical Institute, MA. The PDB entries for the compared structures are 1srl for the c-Src SH3 (*49*), 1nyf for Fyn (*50*), and 1gfc for Grb2 (*51*). Root mean square deviation (rmsd) values for C^α atom positions were measured using InsightII v. 2.3.0. Backbone structure comparisons were made on the basis of C^α-based torsion angles (*52*). C^α torsion angles, $\alpha(i)$, where i is the residue number, were defined as the dihedrals $C^\alpha(i-1)-C^\alpha(i)-C^\alpha(i+1)-C^\alpha(i+2)$ as described by Flocco and Mowbray (*52*). Differences in C^α torsion angles, $\Delta\alpha$, between various proteins were calculated on the basis of aligned SH3 sequences by matching the position of residue i in the two proteins. Sequence numbers in Figure 10 refer to the $C^\alpha(i)$ residues in the Btk SH3.

RESULTS

Analysis of NMR Spectra. Spin system identification and ^1H and ^{15}N resonance assignments were made in DQF−COSY, TOCSY, and TOCSY−HSQC spectra. Sequential resonance assignments were carried out in 150 ms 3D NOESY−HSQC and 150 and 200 ms 2D NOESY spectra using standard methods (*42*, *53*) and, also, using a ^{15}N-edited HSQC-TOCSY−NOESY−HSQC spectrum. Most NOEs were assigned in a 75 ms ^{15}N-edited 3D NOESY−HSQC spectrum and in a 60 ms 2D NOESY spectrum. Some NOEs, in particular those involving aromatic side chains, were assigned in a 60 ms 2D NOESY spectrum recorded on the D_2O sample. No backbone amide resonances in the N-terminal fragment G1−S2−M3−S212 could be detected, and no long-range NOEs involving the eight N-terminal and two C-terminal residues of the protein were observed. Figure 2 shows an assigned ^{15}N HSQC. Unusual ^1H-shifts were observed for two side chains, P265 and S266. The ^1H chemical shifts for S266 are 2.71 ppm (H^α) and 1.83 and 1.62 ppm (H^β), and those for P265 are 3.77 (H^α), 1.16 and 1.01 (H^β), 0.46 and 0.34 (H^γ), and 2.63 and 2.49 (H^δ). All ^1H and ^{15}N chemical shift assignments are available as Supporting Information.

Stereospecific assignments of H^β resonances and identification of predominant χ^1 dihedral angle rotamers were possible for 22 residues. For one of three valines, V220, the $C^\gamma H_3$ resonances were stereospecifically assigned and the side chain χ^1 angle was determined to be in a g^+ conformation. Backbone ϕ dihedral angles were determined for 29 residues. The total number of dihedral angle restraints in the structure calculations was 52, and the number of NOE-derived distance restraints was 756. Most distance restraints involve residues in the structured fragment K217−A272. Eleven hydrogen bonds that fulfilled the criteria described in the Materials and Methods section were found in the analysis of preliminary structures, and these were added as

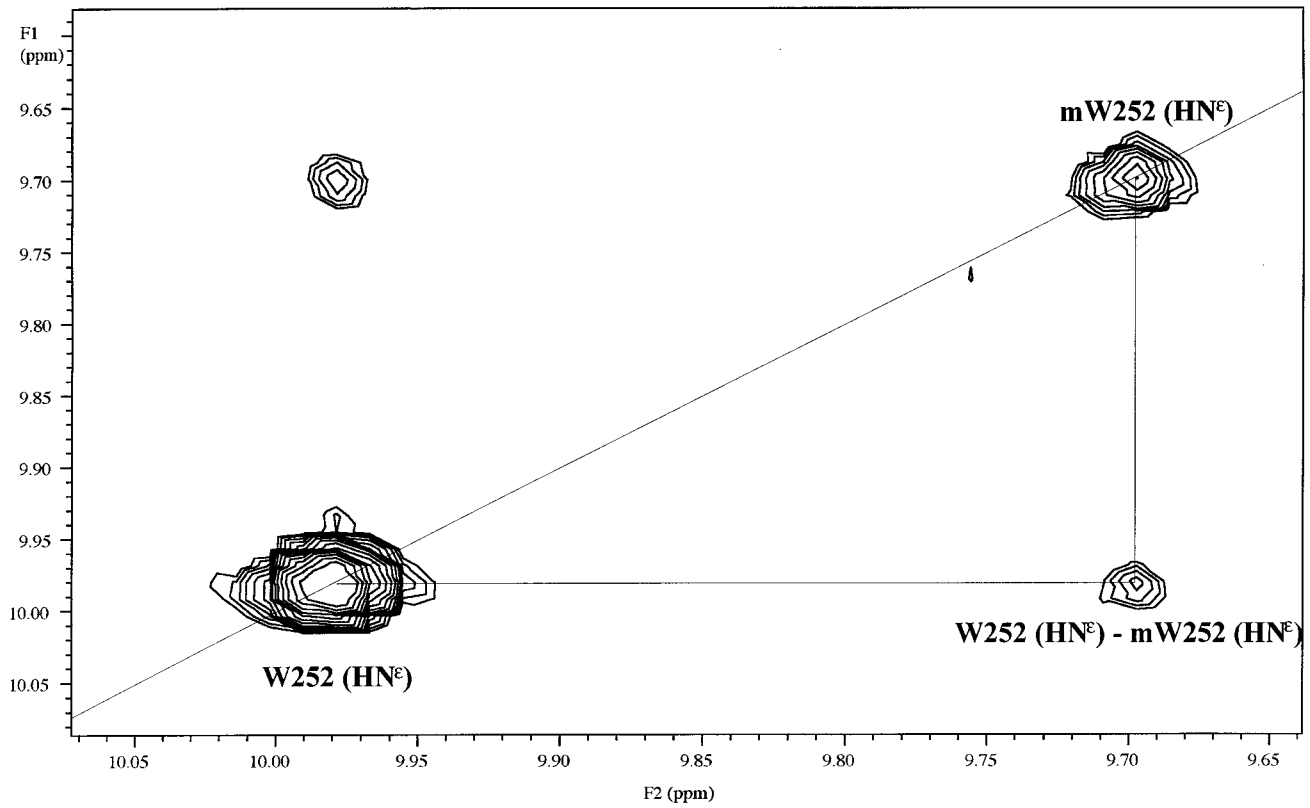

FIGURE 3: Section of a 750 ms 2D NOESY spectrum of Btk SH3 at 50 °C showing the exchange cross-peaks between major and minor (m) form resonances of ^{1}HNe1 in W252.

Table 2: Structural Restraints Summary

total no. of NOE-derived distance restraints	756
intraresidual	297
sequential	196
medium-range	37
long-range	226
total no. of dihedral angle restraints	52
χ^1 dihedral angle restraints	23
backbone ϕ dihedral angle restraints	29
no. of hydrogen bond distance restraints[a]	22

[a] For 11 backbone hydrogen bonds in the β-sheets.

22 hydrogen bond distance restraints. Five additional hydrogen bonds were found in the analysis of the final ⟨SA⟩ ensemble. These are all reported in Table 1. Structural restraints are summarized in Table 2.

Presence of Two Equilibrium Conformations. Several residues in Btk SH3 display two sets of resolved NMR resonances with unequal (major and minor form) intensities. These residues are distributed throughout the protein sequence, although the two forms are not spectroscopically distinguishable within the N- and C-terminal regions or for residues R236−G238 and S247−L249. In the structure, the largest chemical shift differences for backbone amides are within four regions, which are further discussed below. On the basis of relative intensities, we estimate that the concentration ratio of major and minor forms is 7:1. To verify that the observation is due to two conformations of Btk SH3 in equilibrium we recorded long mixing time NOESY spectra at 50 °C. Figure 3 shows the diagonal resonances of the major and minor forms of W252 side-chain ^{1}HN$^\epsilon$1 in a 750 ms NOESY spectrum at 50 °C. Under these conditions we detect exchange cross-peaks between the two diagonal peaks. They indicate the presence of an exchange process between two protein conformations in equilibrium on a time scale of seconds. We have determined the structure of the predominant (major) form of Btk SH3. The low relative concentration of the minor form with accompanying weak NOE intensities prohibits a detailed structural characterization of this form. Still, all NOEs corresponding to the minor form that could be securely assigned are also present in the major form with similar relative intensities. The chemical shift differences between major and minor form resonances are also relatively small with a maximum amide proton shift difference of 0.15 ppm for the amide ^{1}H resonance of M226. These observations suggest that the two forms are structurally similar, as further discussed below.

Structure Calculations. An ensemble of 50 SA structures was calculated as described in Materials and Methods. The distribution of X-PLOR energies of these is shown in Figure 1A, together with the corresponding distance restraint energies (Figure 1B). It is obvious that about 42−44 of the 50 structures have converged to an energetically similar state and that the 6−8 remaining structures are less well refined regarding total and distance restraint violation energies. On the basis of this observation, we have chosen the 42 structures with the lowest total energy as a representative set of the experimentally determined Btk SH3 structure. The structural statistics of this ⟨SA⟩ ensemble is summarized in Table 3. A backbone superposition of structures in ⟨SA⟩ is shown in Figure 4A. The average atomic rmsd of the ⟨SA⟩ structures of Btk SH3 from their mean coordinates is 0.55 Å (±0.16 Å) for the backbone heavy atoms (N, C, C$^\alpha$) and 1.15 Å (±0.15 Å) for all heavy atoms, when analyzed for residues

Table 3: Structural Statistics

	⟨SA⟩[a]	⟨SA⟩$_{av-min}$[b]
rmsd from experimental data		
distance restraints (Å)	0.0363 ± 0.0032	0.0332
dihedral angle restraints (deg)	0.495 ± 0.16	0.345
no. of violations[c]		
distance restraints (>0.3 Å)	1.26	0
dihedral restraints (>3°)	0.12	0
X-PLOR energy	276.3 ± 13.5	243.1
deviations from idealized covalent geometry		
bonds (Å)	0.00376 ± 0.00021	0.00343
angles (deg)	0.680 ± 0.025	0.645
impropers (deg)	0.463 ± 0.019	0.434
atomic rmsd		
backbone atoms[d]	0.55 ± 0.16	
all heavy atoms[d]	1.15 ± 0.15	
Ramachandran plot analysis		
residues in most-favored regions	62.7%	58.8%[e]
residues in additional allowed regions	32.2%	35.3%[e]
residues in generously allowed regions	5.1%	5.9%[e]
residues in disallowed regions	none	none

[a] The ensemble of 42 final structures. [b] The mean structure obtained by averaging the coordinates of the individual structures and minimizing the energy with all restraints applied. [c] Average value for 42 structures. The maximum distance violation is 0.58 Å, and the maximum dihedral angle violation is −7.2°. [d] The final 42 structures vs averaged coordinates when compared for residues K217−E273 (there are no long-range NOE distance restraints and no dihedral angle restraints outside this region). [e] Calculated for non-glycine and non-proline residues within the structured fragment K217−E273.

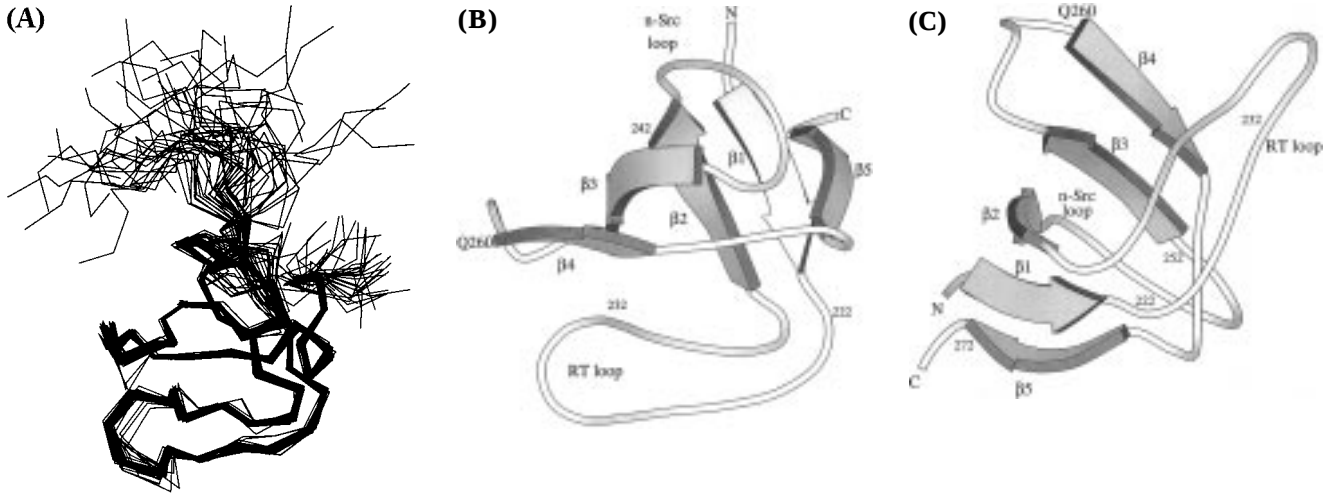

FIGURE 4: (A) Backbone superposition of the ⟨SA⟩ ensemble structures. The structures were aligned with the average structure by the β-strands. The view is the same as in structure B. (B, C) Molscript (*57*) presentations of the backbone conformation in Btk SH3. The β-strand numbering and the location of the RT and n-Src loops have been indicated. The start position (Q260) of the XLA-causing inframe deletion (*11*) is also indicated.

K217−E273. For the β-sheets alone, the rmsd of the 42 structures is 0.41 Å (±0.10 Å) for backbone heavy atoms and 0.92 Å (±0.16 Å) for all heavy atoms. In the potential binding site, defined as residues Y223−D232, W251, S266, and Y268 on the basis of sequence similarities, the rmsd is 0.28 Å (±0.15 Å) for the backbone atoms and 0.79 Å (±0.15 Å) for all heavy atoms. The large difference between the rmsd for backbone and all heavy atoms in the ligand-binding site can be understood because many side chains in this region are exposed on the protein surface and are therefore not well defined by long-range NOE restraints. For residues forming the hydrophobic core in Btk SH3 (identified by inspection), the rmsd for the backbone atoms and for all heavy atoms are 0.20 Å (±0.09 Å) and 0.45 Å (±0.11 Å), respectively. The structures in ⟨*SA*⟩ satisfy the experimental restraints well, as judged by the low number of small distance and dihedral angle restraint violations. The local stereochemistry is also very reasonable, as judged on the basis of average deviations from idealized covalent geometry (Table 3).

Some results from Ramachandran plot analyses of ⟨SA⟩ and of $SA_{ave-min}$ using Procheck-NMR (*47*) are presented in Table 3. A Ramachandran plot of K217−E273 of $SA_{ave-min}$ is shown in Figure 5. There are no residues in disallowed regions of the Ramachandran diagram either for ⟨SA⟩ or for $SA_{ave-min}$. The majority (95.9% for ⟨SA⟩ and 93.2% for $SA_{ave-min}$) of the residues are within most favored or additional allowed regions. Four residues in $SA_{ave-min}$ (M3, A230, E246, and T270) have backbone conformations that fall within generously allowed regions of the Ramachandran diagram. Except for T270, these residues are located in more flexible regions of the protein (see above). For T270, the unfavorable backbone conformation can be explained by a hydrogen bond between its amide proton and

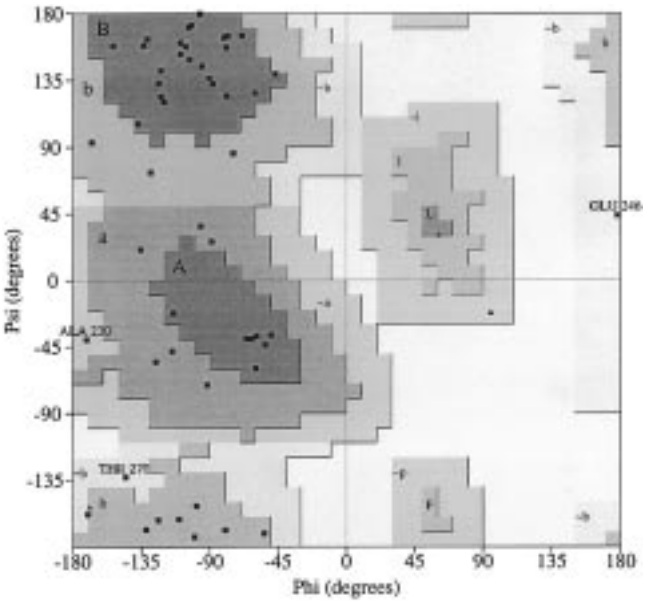

FIGURE 5: Ramachandran diagram of Btk SH3 ($SA_{ave-min}$). Residues in generously allowed regions are indicated (and discussed in the text). The different shading refers to most favored regions (A, B, and L) in darkest gray, additional allowed regions (a, b and l) in dark gray, generously allowed regions in light grey, and disallowed regions in white. The diagram was produced with Procheck-NMR (*47*).

the backbone carbonyl oxygen of V220 (Table 1). Excluding glycines, positive ϕ dihedral angles are observed for M3 and E246 in $SA_{ave-min}$. Both these residues are located in more flexible regions.

Backbone Dynamics. The generalized order parameters for backbone dynamics (S^2), determined on the basis of R_1, R_2, and $\{^1H\}^{15}N$ steady-state NOE measurements, are plotted on a per-residue basis in Figure 6A. S^2 can be interpreted as the degree of restriction of the NH bond vector on a time scale characterized by the internal correlation time, which is shorter than the correlation time for rotational diffusion of the entire protein. S^2 ranges from 0 for completely unrestricted internal motion to 1 in the absence of internal motions. Considering these data, the structured domain of Btk SH3 seems to be from residue K217 to A272. With some exceptions these residues all have high values of S^2, whereas the eight N-terminal and three C-terminal residues are more flexible. Conformational flexibility in the N- and C-terminal regions explains the high atomic rmsd (Figure 6B) and low angular order parameters obtained for ϕ and ψ dihedral angles (S^ϕ and S^ψ; Figures 6C and 6D) for these residues. As already mentioned, no long-range NOEs were observed for the eight N-terminal and two C-terminal residues (Figure 6E).

There are two additional regions within the otherwise structured domain that seem to be flexible, where lower S^2 values correspond to lower S^ϕ and S^ψ values and higher rmsd. These are residues M228−N229 and S247−N248 (relaxation measurements were not possible for A230 and E246, due to spectral overlap). Both regions are surface-exposed and are located within the RT and n-Src loops, respectively. Two additional regions, residues R236−K237 and K257−N258−G259, show some disorder among the calculated structures as judged from backbone rmsd, S^ϕ, and S^ψ. In the structure R236−K237−G238 form a turn (resembling a Type II β-turn) and K257−N258−G259 a turn-like loop. The low values of S^ϕ and S^ψ do not correspond to low S^2, though the intensity of the $\{^1H\}^{15}N$ steady-state NOE for residue N258 (data not shown) is somewhat lower than in the structured domain (spectral overlap prohibits relaxation measurements on K257). The number of NOEs defining these two regions is low. Thus, these parts of the structure are less well determined, based on the structure calculations, but not inherently flexible on the pico- to nanosecond time scales.

Description of the Structure. The structured part of Btk SH3 consists of five β-strands that are packed in two β-sheets forming a β-sandwich, typical for SH3 domains (Figures 4B and 4C). The first β-strand, β1, starts with the K217 and ends with A221. L222−G238 forms the RT loop, with the highly conserved Y223 at the edge of the potential binding site and the nonconserved M228−N229−A230 forming a flexible, turnlike part of this loop at the other end of the binding site. The fragments D224−P227 and D232−L235 run antiparallel to each other and form a well-defined segment of the RT loop. The backbone amide proton of L235 forms hydrogen bonds with the backbone carbonyl of Y225 and L233. Residues R236−K237−G238 form a turn that resembles a Type II β-turn, but the conformation could not be securely defined due to spectral overlap involving crucial NOEs. This sequence is partially conserved among different SH3 domains (Figure 7), and in c-Src SH3 it forms a Type II β-turn (49). The second β-strand, β2, consists of five residues: D239, E240, Y241, F242, and I243. D239−F242 is antiparallel to β1, and Y241−I243 is antiparallel to A254−D256 within the third β-strand, β3, which consists of residues R253 to D256. The backbone amide protons of Y241 and F242 form hydrogen bonds with backbone carbonyls of V219 and R255, respectively. The partially flexible loop between β2 and β3 corresponds to the n-Src loop. The fourth β-strand, β4, is formed by residues Q260, E261, G262, and Y263. β3 and β4 run antiparallel to each other with hydrogen bonds between A254 and G263 and between D256 and Q260 and, also, between P250 and S266 and between W252 and I264. Residues K257, N258, and G259 form a turnlike loop between β3 and β4. S266, N267, and Y268 are all highly conserved among SH3 domains and form a right-handed helix-like loop between β4 and the fifth β-strand, β5 consisting of residues V269, T270, and E271. β5 is antiparallel to β1 with a hydrogen bond between V220 and T270.

A surface analysis of Btk SH3 reveals that 56% of the total surface area, 5292 Å^2, is polar. The hydrophobic core consists of residues V219, L233, L235, Y241, I243, A254, I264, and V269, which are well conserved among SH3 domains. The surface of the potential binding site involves the conserved residues Y223, D224, Y225, D232, W251, P265, and Y268 (see Lim et al. (*54*) for a discussion about binding sites in SH3 domains). They form a continuous surface as illustrated in Figure 8. The autophosphorylated Y223 is located at one end of this surface, and the other side is flanked by residues in the partially flexible RT loop. Several other hydrophobic side chains are exposed or partially exposed on the surface, including V220, L222, M226, P227, M228, F242, L244, L249, and P250.

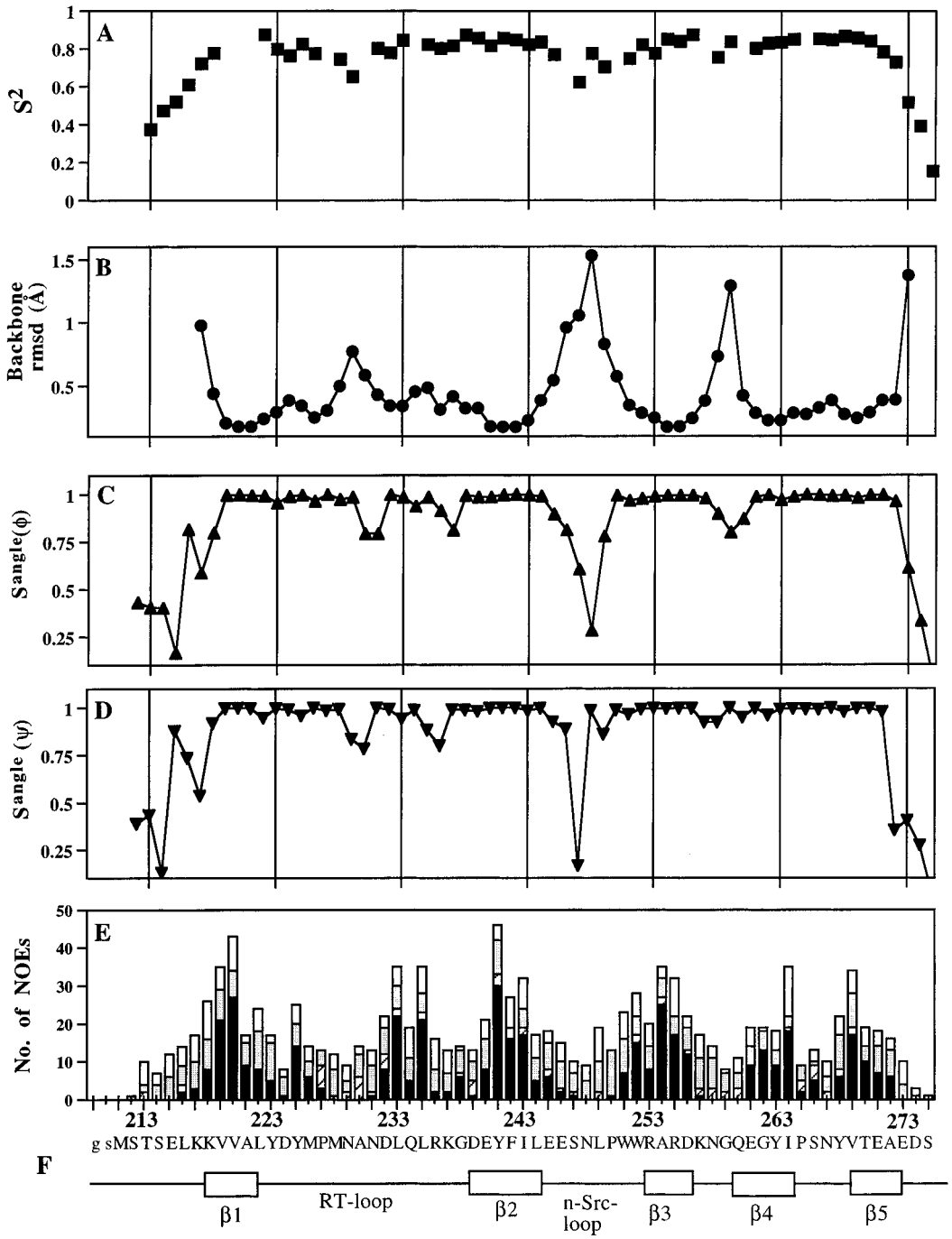

FIGURE 6: (A) Amplitudes of rapid backbone dynamics represented by the generalized order parameter, S^2. (B) Average rmsd for backbone heavy atoms of 42 structures. (C, D) Angular order parameters, S^{angle}, for backbone torsion angles ϕ and ψ. (E) Distribution of NOE restraints. The height and shading of the bars reflect the number and class of NOE-derived restraints, respectively. White, intraresidue NOE restraints; gray, sequential NOE restraints; staples, medium-range NOE restraints; and black, long-range NOE restraints. (F) Sequence and secondary structure elements in Btk SH3.

DISCUSSION

In the present study we have determined the solution structure of the Btk SH3 and have also investigated dynamic properties. The precision of the calculated structures is good as judged from rmsd from mean coordinates and the local stereochemistry is also very reasonable. The lower precision obtained for certain regions, e.g. the RT and n-Src loops, can in most cases be attributed to rapid internal motions or surface exposure. Below we discuss the origin of the observed slow conformational exchange, the functional role of the autophosphorylated Y223 residue and compare the Btk SH3 structure with the structures of some other SH3 domains.

Mechanism for Conformational Exchange. The existence of two conformations of Btk SH3 in solution is apparent, though the biological relevance of this, if any, is unclear. The backbone conformations of major (predominant) and minor forms appear to be quite similar. This is because the chemical shift differences are small and because observed backbone amide NOEs for the minor form are similar to those of the major form. The largest backbone shift differences are found within four distinct regions of the

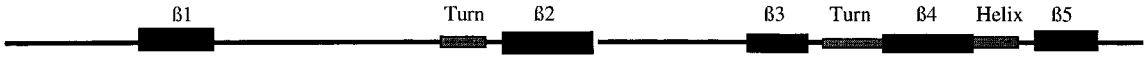


```
SH3-domain  218        228        238        248        258        268      275
Btk:gsmstselKK VVALYDYMPM NANDLQLRKG DEYFILEES_N LPWWRARD_KN GQEGYIPSNY VTEAEds
Itk:       eeTL VIALYDYQTN DPQELALRCD EEYYLLDSS_E IHWWRVQD_KN GHEGYAPSSY LVE
c-Src:  aggvtt FVALYDYESR TETDLSFKKG ERLQIVNNT_E GDWWLAHSLTT GQTGYIPSNY VAP
Fyn:       gvTL FVALYDYEAR TEDDLSFHKG EKFQILNSS_E GDWWEARSLTT GETGYIPSNY VAP
Grb2        sTY VQALFDFDPQ EDGELGFRRG DFIHVMDNS_D PNWWKGA__CH GQTGMFPRNY VTPVN
Lck:       QDNL VIALHSYEPS HDGDLGFEKG EQLRILEQS__ GEWWKAQSLTT GQEGFIPFNF VAKANS
Abl:          L FVALYDFVAS GDNTLSITKG EKLRVLGYNHN GEWCEAQT_KN GQ_GWVPSNY ITPV
```

FIGURE 7: (A) Sequence alignment of Btk SH3 domain with the SH3 domains from Itk, c-Src, Abl, Grb-2, Fyn, and Lck. The numbering refers to Btk. Lower case letters in Btk, Src, and Fyn represent residues that were not used in the structural comparison (Figure 10).

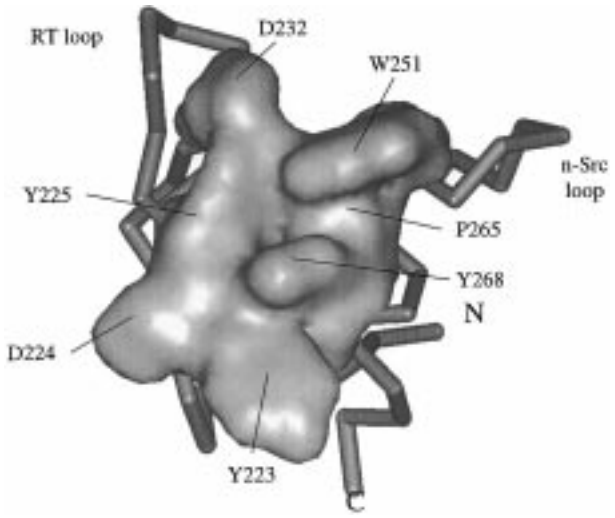

FIGURE 8: Surface representation of amino acid residues forming the potential binding site in Btk SH3. A backbone trace with the location of the RT and n-Src loops is also shown. The picture was produced using a Preview Edition of WebLab ViewerPlus from Molecular Simulations Inc.

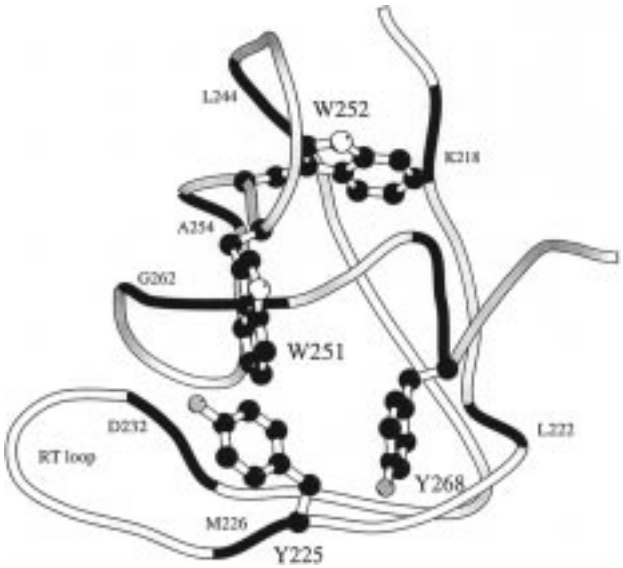

FIGURE 9: Backbone trace of Btk SH3. Regions with the largest chemical shift differences between the major and minor forms are colored in black. Indicated and displayed are also the side chains of Y225, W251, W252, and Y268. Residues with large chemical shift differences are K218 (Δ^{15}N, 0.38 ppm; ΔNH, 0.01 ppm), L222 (0.19 ppm, 0.04 ppm), Y225 (0.03 ppm, 0.05 ppm), M226 (0.40 ppm, 0.15 ppm) D232 (0.09 ppm, 0.06 ppm), L233 (0.19 ppm, 0.07 ppm), L244 (0.23 ppm, 0.20 ppm), E245 (0.08 ppm, 0.15 ppm), A254 (0.92 ppm, 0.08 ppm), D256 (0.31 ppm, 0.04 ppm), G262 (0.68 ppm, 0.02 ppm), Y263 (0.16 ppm, 0.06 ppm), I264 (0.36 ppm, 0.11 ppm), and Y268 (0.32 ppm, 0.10 ppm).

structure, as illustrated in Figure 9. These regions are residues M226, D232, and L233 within the RT loop (I), G262−I264 in β4 and A254 in β3 (II), N267 and Y268 within the helix-like loop and L222 (III), and residues L244 and E245 within the n-Src loop (IV).

The exchange between the two conformations occurs on a time scale of seconds. Intramolecular conformational exchange on this time scale has been attributed to proline *cis*−*trans* isomerizations (see e.g. ref (55) and slow reorientations of tryptophan aromatic rings (*56*). These mechanisms appear most plausible, although other possibilities cannot be excluded. Btk SH3 contains three proline (P227, P250, and P265) and two tryptophan residues (W251 and W252). If we first consider proline *cis*−*trans* isomerization, this mechanism cannot involve P250, because backbone resonances around this proline exhibit only very small shift differences between the two forms. P227 is located quite far from most of the residues with large backbone shift differences. For P265 we observe minor form NOEs between the H^{α} of I264 and $H^{\delta}1$ and $H^{\delta}2$ of P265 (data not shown), indicating that the minor form conformation of P265 is trans as in the major form. Thus, proline *cis*−*trans* isomerization is not likely to be the cause of the conformational exchange.

A tryptophan side chain reorientation or "flip" results in multiple protein conformations e.g. in the human α3-chain type VI collagen C-terminal Kunitz domain (*56*). The exchange rate was also in this case found to be rather slow (1.0 s^{-1}). In Btk SH3, the side chains of W251 and W252 both display rather large major/minor form chemical shift differences. A reorientation of the W251 aromatic ring can easily affect parts of the RT loop via the closely located Y225 side chain. Also the side chain of Y268 is close to W251 and could mediate conformational changes to the backbone around Y268 and L222. Residues G262−I264 in β4 are located near the aromatic ring of W251. Finally, the fourth region within the n-Src loop is located close to W252. A reorientation of W251 aromatic ring would most likely also affect the aromatic ring of W252, which then can affect part of the nearby n-Src loop. Thus, on the basis of the location of observed shift differences in relation to the W251 side chain, we favor a reorientation of this aromatic ring as the most likely cause of the conformational exchange in Btk SH3.

Comparison of the Btk SH3 Structure with Other SH3 Domains. Figure 7 shows a sequence alignment of the Btk SH3 domain with Itk, c-Src, Abl, Grb-2-N, Fyn, and Lck SH3 domains. The degree of conservation is highest compared to the Tec family Itk SH3 in which 29 of 56

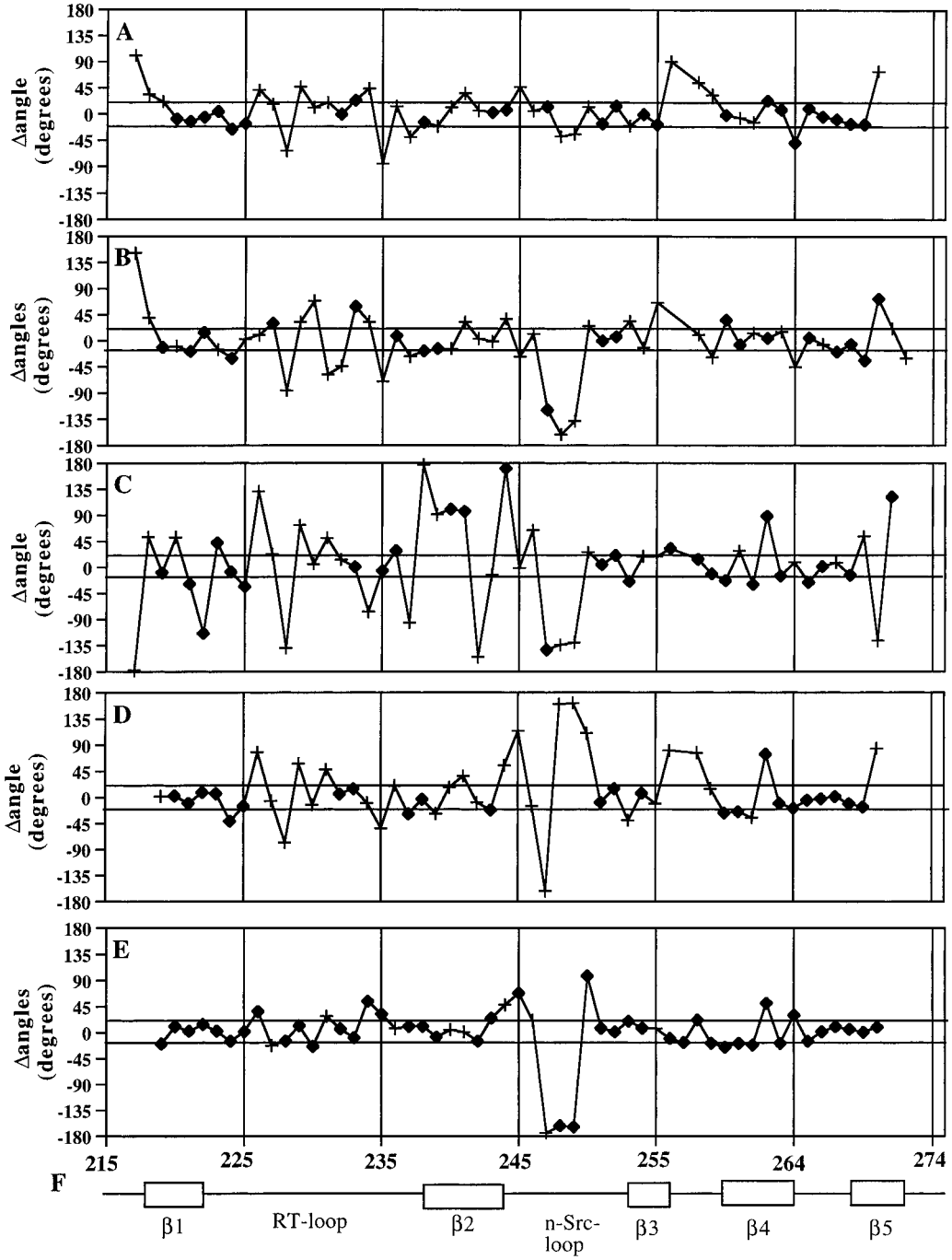

FIGURE 10: Comparison of backbone C^{α} torsion angles in Btk SH3 and the SH3 domains of Itk, Src, Fyn, and Grb-2. This dihedral angle was defined and measured according to Flocco and Mowbray (*52*). Differences in C^{α} torsion angles, Δangle, between the structures are plotted by residue with crosses or filled diamonds, where the latter correspond to conserved positions. The numbering refers to Btk SH3. (A) Btk SH3 vs Fyn SH3. (B) Btk SH3 vs Grb2 SH3. (C) Btk SH3 vs Itk SH3. (D) Btk SH3 vs Src SH3. (E) Fyn SH3 vs Src. (F) secondary structural elements of Btk SH3.

residues are identical with Btk SH3. In comparison, c-Src SH3 has 24 residues in common with Btk SH3 and 43 with Fyn SH3. Figure 10 shows a comparison of backbone conformations of Btk SH3 with the other domains. The comparison is based on backbone C^{α} dihedral angles (*52*). In this comparison, the Fyn and c-Src SH3 domains, both belonging to the Src family of tyrosine kinases, form the most "look-alike" pair (Figure 10E). The Btk SH3 backbone conformation is actually more similar to both Fyn and c-Src than to the Itk SH3, although the latter is the only SH3 structure from another Tec family kinase. These differences/similarities are also apparent from superpositions of backbone atoms: the rmsd between 432 superimposed backbone atoms (backbone atoms of 54 common residues) are 1.82 and 1.39 Å for Btk−c-Src and Btk−Fyn, respectively, but 2.54 Å in a Btk−Itk comparison. The corresponding number for a c-Src−Fyn superposition is 1.44 Å.

Continuing the comparison between the Btk and the c-Src and Fyn SH3 domains, we find only minor differences in backbone conformations except for in the RT loop, the n-Src loop (of c-Src), and the turn between β-strands 3 and 4. Notably, the n-Src loop conformation is very similar in Btk and Fyn but is different in Btk and c-Src (and in Fyn and c-Src). The conformation of the RT loop in Btk is altered

compared to Fyn and c-Src, where the loop takes very similar conformations. The residues of Fyn and c-Src that correspond to S266−Y268 in Btk form a short right-handed 3_{10} helix in these proteins, and a similar conformation is found in Btk.

We also find that the backbone conformation of a previously published model of Btk SH3 (*11*) compares well with the presently determined structure, except for a few residues in the n-Src loop. Thus, differences in the backbone conformation between the Btk SH3 model and the NMR structure are smaller than the differences between the experimentally determined Fyn and Btk SH3 structures (not shown).

The observed structural differences between the Itk and Btk SH3 domains are somewhat unexpected. The two proteins obviously have similar overall folds, but significant differences in backbone conformations can be found in the N-terminal, the RT loop, the β2-strand, and in the n-Src loop. The differences may be attributed to the fact that the Itk fragment, for which the structure was determined, is extended in the N-terminal compared to the other SH3 domains. The N-terminal extension, which contains an SH3 polyproline binding motif, interacts with the binding site (*17*). The difference between the two Tec family SH3 domains and the similarity between Btk and SH3 domains in kinases and other signaling molecules suggest that ligand binding may alter the SH3 conformation in Tec family kinases, but additional studies are required to draw this conclusion.

Structure and Function of Btk SH3. Bruton's tyrosine kinase has been shown to be activated through a transphosphorylation of Y551 within the kinase domain, followed by autophosphorylation of Y223 within the SH3 domain (*22*). In our structure, Y223 is exposed on the surface at the edge of the binding site (Figure 8). A phosphorylation provides a negative charge (as well as a steric exclusion) to this region which can be severely unfavorable for the interaction with a ligand.

In the c-Src family tyrosine kinase Hck, a displacement of the SH3 domain occurs upon activation (*20*) confirming the key role of SH3 domains in regulation of tyrosine kinases. Recently, the crystal structures of inactivated Hck and c-Src kinases were solved (*18*, *19*). In these structures the linker connecting the SH2 domain with the kinase domain acts as an intramolecular ligand for the SH3 domain. This is also a plausible mechanism for Btk regulation. Most of the binding surfaces of SH3 domains consist of conserved residues, mainly three tyrosines (Y223, Y225, and Y268 in Btk), one aspartate (D232 in Btk) and one tryptophan (W251 in Btk). Isolated peptide ligands also show a high degree of sequence homology. The residues involved in forming the (intramolecular) SH3 ligand, a left-handed PPII helix, are in c-Src residues K249−Q253 (KPQTQ), followed by G254 and L255, and in Hck as residues K249−W254 (KPQKPW). Corresponding residues in Btk are A384−L390 (APSTAGL), which can be derived from an alignment of the Btk kinase domain with those of Hck and c-Src.

In the interaction between SH3 domains and peptide ligands there are five positions on the ligand surface where close contacts with residues on the SH3 domain are formed: P_{+3}, P_{+2}, P_0, P_{-1}, and P_{-3} (for the notation, see Lim et al. (*54*)). The P_{+3} position is normally occupied by a hydrophobic residue in SH3-binding peptides, most often a proline or an alanine. In both c-Src and Hck this position is occupied by a lysine (K249), though the corresponding residue in Btk is an alanine (A384). The P_{+2} position is held by P250 in the c-Src and Hck crystal structures. This critical residue is conserved also in other tyrosine kinases, as well as in Btk (P385), and is a proline also in SH3 binding peptides. The P_0 position, which is a valine or leucine in many SH3-binding peptides, is a lysine (K252) in Hck and a threonine (T252) in c-Src. In Btk it is a threonine, T387. The P_{-1} position is held by P253 in Hck and Q253 in c-Src. The corresponding Btk residue is an alanine (A388). The P_{-3} position in SH3-binding peptides is normally held by a basic residue, which contacts the conserved aspartate in the binding pocket. This interaction is absent in both c-Src and Hck. Residues G254 and L255 of c-Src are present also in Btk: G389 and L390. Thus, the region of Btk which corresponds to the SH2-kinase linkers that bind to SH3 in the c-Src and Hck complexes is similar at many of the critical positions. At one place, where there is no similarity, the corresponding Btk residue is instead conserved compared to other known SH3-binding peptides. Thus, the Btk sequence supports the notion that intramolecular interactions of the SH3 domain, similar to those observed in c-Src and Hck, may be involved in the regulation of Btk function.

ACKNOWLEDGMENT

The authors gratefully acknowledge Amy H. Andreotti for kindly providing the coordinates for the Itk SH3 structure and Patricia Humire for technical help.

SUPPORTING INFORMATION AVAILABLE

Table of the ^{1}H and ^{15}N chemical shift assignments (in ppm) in Btk SH3 (5 pages). Ordering information is given on any current masthead page.

REFERENCES

1. Sideras, P., and Smith, C. I. E. (1995) *Adv. Immunol. 59*, 135−223.
2. Tsukada, S., Saffran, D. C., Rawlings, D. J., Parolini, O., Allen, R. C., Klisak, I., Sparkes, R. S., Kubagawa, H., Mohandas, T., Quan, S., Belmont, J. W., Cooper, M. D., Conley, M. E., and Witte, O. N. (1993) *Cell 72*, 279−290.
3. Vetrie, D., Vorechovsky, I., Sideras, P., Holland, J., Davies, A., Flinter, F., Hammarström, L., Kinnon, C., Levinsky, R., Bobrow, M., Smith, C. I. E., and Bentley, D. R. (1993) *Nature 361*, 226−233.
4. de Weers, M., Verschuren, M. C. M., Kraakman, M. E. M., Mensink, R. G. J., Schuurman, R. K. B., van Dongen, J. J. M., and Hendriks, R. W. (1993) *Eur. J. Immunol. 23*, 3109−3114.
5. Smith, C. I. E., Baskin, B., Humire-Greiff, P., Zhou, J.-N., Olsson, P. G., Maniar, H. S., Kjellén, P., Lambris, J. D., Christensson, B., Hammarström, L., Bentley, D., Vetrie, D., Islam, K. B., Vorechovsky, I., and Sideras, P. (1994) *J. Immunol. 152*, 557−565.
6. Smith, C. I. E., Islam, K. B., Vorechovsky, I., Olerup, O., Wallin, E., Rabbani, H., Baskin, B., and Hammarström, L. (1994) *Immunol. Rev. 138*, 159−183.
7. Shaw, G. (1993) *Biochem. Biophys. Res. Commun. 195*, 1145−1151.
8. Salim, K., Bottomley, M. J., Querfurth, E., Zvelebil, M. J., Gout, I., Scaife, R., Margolis, R. L., Gigg, R., Smith, C. I. E., Driscoll, P. C., Waterfield, M. D., and Panayotou, G. (1996) *EMBO J. 15*, 6241−6250.
9. Vihinen, M., Nilsson, L., and Smith, C. I. E. (1994) *FEBS Lett. 350*, 263−265.

10. Vihinen, M., Belohradsky, B. H., Haire, R. N., Holinski-Feder, E., Kwan, S.-P., Lappalainen, I., Lehväslaiho, H., Lester, T., Meindl, A., Ochs, H. D., Ollila, J., Vorechovsky, I., Weiss, M., and Smith, C. I. E. (1997) *Nucleic Acids Res. 25*, 166−171.
11. Zhu, Q., Zhang, M., Rawlings, D. J., Vihinen, M., Hagemann, T., Saffran, D. C., Kwan, S.-P., Nilsson, L., Smith, C. I. E., Witte, O. N., Chen, S.-H., and Ochs, H. D. (1994) *J. Exp. Med. 180*, 461−470.
12. Chen, Y.-J., Lin, S.-C., Tzeng, S.-R., Patel, H. V., Lyu, P.-C., and Cheng, J.-W. (1996) *Proteins 26*, 465−471.
13. Ren, R., Mayer, B. J., Cicchetti, P., and Baltimore, D. (1993) *Science 259*, 1157−1161.
14. Yu, H., Chen, J. K., Feng, S., Dalgarno, D. C., Brauer, A. W., and Schreiber, S. L. (1994) *Cell 76*, 933−945.
15. Cheng, G., Ye, Z.-S., and Baltimore, D. (1994) *Proc. Natl. Acad. Sci. U.S.A. 91*, 8152−8155.
16. Bunnell, S. C., Henry, P. A., Kolluri, R., Kirchhausen, T., Rickles, R. J., and Berg, L. J. (1996) *J. Biol. Chem. 271*, 25646−25656.
17. Andreotti, A. H., Bunnell, S. C., Feng, S., Berg, L. J., and Schreiber, S. L. (1997) *Nature 385*, 93−97.
18. Sicheri, F., Moarefi, I., and Kuriyan, J. (1997) *Nature 385*, 602−609.
19. Xu, W., Harrison, S. C., and Eck, M. J. (1997) *Nature 385*, 595−602.
20. Moarefi, I., LaFevre-Bernt, M., Sicheri, F., Huse, M., Lee, C.-H., Kuriyan, J., and Miller, W. T. (1997) *Nature 385*, 650−653.
21. Rawlings, D. J., Scharenberg, A. M., Park, H., Wahl, M. I., Lin, S., Kato, R. M., Fluckiger, A.-C., Witte, O. N., and Kinet, J.-P. (1996) *Science 271*, 822−825.
22. Park, H., Wahl, M. I., Afar, D. E. H., Turck, C. W., Rawlings, D. J., Tam, C., Scharenberg, A. M., Kinet, J.-P., and Witte, O. N. (1996) *Immunity 4*, 515−525.
23. Bullock, W. O., Fernandez, J. M., and Short, J. M. (1987) *BioTechniques 5*, 376−378.
24. Bradford, M. M. (1976) *Anal. Biochem. 72*, 248−254.
25. Levy, G. C., and Lichter, R. L. (1979) in *Nitrogen-15 Nuclear Magnetic Resonance Spectroscopy* (Levy, G. C., and Lichter, R. L., Ed.) pp 59, Wiley, New York.
26. Rance, M., Sørensen, O. W., Bodenhausen, G., Wagner, G., Ernst, R. R., and Wüthrich, K. (1983) *Biochem. Biophys. Res. Commun. 117*, 479−485.
27. Macura, S., and Ernst, R. R. (1980) *Mol. Phys. 41*, 95−117.
28. Griesinger, C., Otting, G., Wüthrich, K., and Ernst, R. R. (1988) *J. Am. Chem. Soc. 110*, 7870−7872.
29. Lippens, G., Dhalluin, C., and Wieruszeski, J.-M. (1995) *J. Biomol. NMR 5*, 327−331.
30. Marion, D., Ikura, M., Tschudin, R., and Bax, A. (1989) *J. Magn. Reson. 85*, 393−399.
31. Kay, L. E., Keifer, P., and Saarinen, T. (1992) *J. Am. Chem. Soc. 114*, 10663−10665.
32. Zhang, O., Kay, L. E., Olivier, J. P., and Forman-Kay, J. D. (1994) *J. Biomol. NMR 4*, 845−858.
33. Kuboniwa, H., Grzesiek, S., Delaglio, F., and Bax, A. (1994) *J. Biomol. NMR 4*, 871−878.
34. Archer, S. J., Ikura, M., Torchia, D. A., and Bax, A. (1991) *J. Magn. Reson. 95*, 636−641.
35. Farrow, N. A., Muhandiram, R., Singer, A. U., Pascal, S. M., Kay, C. M., Gish, G., Shoelson, S. E., Pawson, T., Forman-Kay, J. D., and Kay, L. E. (1994) *Biochemistry 33*, 5984−6003.
36. Kraulis, P. J. (1989) *J. Magn. Reson. 84*, 627−633.
37. Kraulis, P. J., Domaille, P. J., Campbell-Burke, S. L., van Aken, T., and Laue, E. D. (1994) *Biochemistry 33*, 3515−3531.
38. Palmer, A. G., III, Rance, M., and Wright, P. E. (1991) *J. Am. Chem. Soc. 113*, 4371−4380.
39. Peng, J. W., and Wagner, G. (1994) *Methods Enzymol. 239*, 563−596.
40. Lipari, G., and Szabo, A. (1982) *J. Am. Chem. Soc. 104*, 4546−4559.
41. Lipari, G., and Szabo, A. (1982) *J. Am. Chem. Soc. 104*, 4559−4570.
42. Wüthrich, K. (1986) NMR of Proteins and Nucleic Acids, John Wiley & Sons: New York.
43. Fletcher, C. M., Jones, D. N. M., Diamond, R., and Neuhaus, D. (1996) *J. Biomol. NMR 8*, 292−310.
44. Vuister, G. W., and Bax, A. (1993) *J. Am. Chem. Soc. 115*, 7772−7777.
45. Wagner, G., Hyberts, S. G., and Havel, T. F. (1992) *Annu. Rev. Biophys. Biomol. Struct. 21*, 167−198.
46. Brünger, A. T. (1992) X.-PLOR version 3.1. A System for X-ray Crystallography and NMR, 3.1 ed., Yale University Press: New Haven, CT.
47. Laskowski, R. A., Rullmann, J. A. C., MacArthur, M. W., Kaptein, R., and Thornton, J. M. (1996) *J. Biomol. NMR 8*, 477−486.
48. Hyberts, S. G., Goldberg, M. S., Havel, T. F., and Wagner, G. (1992) *Protein Sci. 1*, 736−751.
49. Yu, H., Rosen, M. K., Shin, T. B., Seidel-Dugan, C., Brugge, J. S., and Schreiber, S. L. (1992) *Science 258*, 1665−1668.
50. Morton, C. J., Pugh, D. J. R., Brown, E. L. J., Kahmann, J. D., Renzoni, D. A. C., and Campbell, I. D. (1996) *Structure 4*, 705−714.
51. Kohda, D., Terasawa, H., Ichikawa, S., Ogura, K., Hatanaka, H., Mandiyan, V., Ullrich, A., Schlessinger, J., and Inagaki, F. (1994) *Structure 2*, 1029−1040.
52. Flocco, M. M., and Mowbray, S. L. (1995) *Protein Sci. 4*, 2118−2122.
53. Marion, D., Driscoll, P. C., Kay, L. E., Wingfield, P. T., Bax, A., Gronenborn, A. M., and Clore, G. M. (1989) *Biochemistry 28*, 6150−6156.
54. Lim, W. A., Richards, F. M., and Fox, R. O. (1994) *Nature 372*, 375−379.
55. Chazin, W. J., Kördel, J., Drakenberg, T., Thulin, E., Brodin, P., and Grundström, T. (1989) *Proc. Natl. Acad. Sci. U.S.A. 86*, 2195−2198.
56. Dahl Sørensen, M., Kristensen, S. M., Bjørn, S., Norris, K., Olsen, O., and Led, J. J. (1996) *J. Biomol. NMR 8*, 391−403.
57. Kraulis, P. J. (1991) *J. Appl. Crystallogr. 24*, 946−950.

BI972409F